Int J Adv Manuf Technol (2015) 77:1177–1189
DOI 10.1007/s00170-014-6514-z

ORIGINAL ARTICLE

Process models for controlled-depth abrasive waterjet milling of amorphous glasses

Thai Nguyen · Jun Wang · Weiyi Li

Received: 2 September 2014 / Accepted: 17 October 2014 / Published online: 6 November 2014
© Springer-Verlag London 2014

Abstract An abrasive waterjet milling technique has been developed to machine brittle amorphous glass in a controlled-depth milling mode, without using sacrificed masking plates made of hard materials. The main mechanisms associated with the milled channel formation process, i.e. the particle impact erosion, jet flow characteristics and the dynamics of nozzle motion, are analysed to arrive at the models for predicting the material removal rate and the geometry of the channels milled by this technique. It is found that these milling performance quantities are dominated by nine dimensionless variables representing the processing parameters and material properties that govern the major mechanisms involved in the milled channel formation. An experimental verification has been carried out and shows that the model predictions are in good agreement with the corresponding experimental data.

Keywords Abrasive waterjet · Controlled-depth milling · Predictive model · Erosion · Jet characteristics · Nozzle motion dynamics

Nomenclature

A	Cross-sectional area of the milled channel (m^2)
A_0, A_1, A_2	Cross-sectional area of the portions shown in Fig. 3 (m^2)
a	Maximum acceleration of a robot hand (m/s^2)
b	Sliding distance due to the impact of a particle (mm)
C_D	Modelling coefficient in Eq. (39)
C_d	Discharge coefficient
C	Coefficient considering the response of material to a particle impact under elastic–plastic deformation
C_m	Momentum transfer efficiency
C_p	Particle concentration in slurry
C_s	Jet velocity reduction factor
C_Φ	Modelling coefficient in Eq. (40)
D	Depth of channel (mm)
d_j	AWJ diameter (mm)
d_n	Diameter of the nozzle at the outlet (mm) (Fig. 7)
d_p	Nominal particle diameter (mm)
E	Young modulus of material (MPa)
$\vec{F}$	Resultant external force acting on the jet (N)
f	Cross feed (mm)
H	Hardness of material (MPa)
h	Penetration depth due to the impact of a particle (mm)
K	Fracture toughness of material ($MPa.m^{1/2}$)
K_μ	Consistency index of slurry ($N/m^2.s^n$)
k	Number of particles occupying within the cross section of a jet
dKE/dt	Rate of kinetic energy (W)
L	Milled channel length (mm)
MRR	Material removal rate (mm^3/s)
m_p	Mass of a particle (kg)
$\dot{m}_p$	Mass flow rate of particles ejecting through the nozzle (kg/s)
$\dot{m}_w$	Mass flow rate of water ejecting through the nozzle (kg/s)
$\dot{n}$	Rate of number of particles ejecting through the nozzle (s^{-1})
n	Flow behaviour index of slurry
P	Water pressure (MPa)
Re	Reynolds number
S	Standoff distance (mm)

T. Nguyen · J. Wang (✉) · W. Li
School of Mechanical and Manufacturing Engineering, UNSW Australia (The University of New South Wales), Sydney NSW 2052, Australia
e-mail: jun.wang@unsw.edu.au

t_o	Time required for milling a unit length of channel in the X direction (m)
u	Nozzle traverse speed (mm/s)
V_i	Volume of material removed by the impact of one particle (mm^3)
v_p	Particle velocity (m/s)
$\overline{v}_j$	Average AWJ velocity distributed across the jet section (m/s)
$\overline{v}_w$	Average water velocity flowing through the orifice of a nozzle system (m/s)
W	Actual top width of the milled channels (mm)
w	Programmed width of the milled channel (mm)

Greek symbols

a	Nozzle tilted angle in the models (deg or rad)
α_p	Impact angle of a particle (deg or rad)
$\dot{\gamma}$	Shear rate in slurry (s^{-1})
δ	Ductility index of material
ς_i	Exponents in Eq. (39)
ρ_w	Density of water (kg/m^3)
ρ_s	Density of slurry (kg/m^3)
ϕ	Channel's wall inclination angle in the models (rad)
μ_w	Dynamic viscosity of water (Pa.s)
φ	Jet deflection angle (rad)
φ_p	Deflection angle in trajectory of a particle (deg or rad)
ψ_m	Momentum transfer efficiency
ψ_c	Coefficient accounting for the number of active particles
ψ_u	Coefficient accounting for the effect of nozzle motion
ψ_v	Coefficient accounting for the variation of particle velocity within a jet
ς_i	Exponents in Eq. (40)

1 Introduction

An abrasive waterjet (AWJ) allows the kinetic energy from an ultra-high pressurised water source to be transferred to various tinny abrasive particles for cutting applications. Unlike the use of solid cutting tools where the convective cooling is mostly restricted outside the tool-workpiece interface [1], in AWJ machining the continuous flow of the jet passing through the cutting target allows the heat generated and the swarf resulted from the material removal to be sufficiently carried away [2]. As a result, AWJ cutting has been found to be a capable method for processing various materials; examples include the work by Momber and Kovacevi [3] on cutting rubbers, Arola et al. [4] on cutting titanium alloys and Wang [5, 6] on cutting polymer matrix composites and ceramics. All these materials are difficult to machine by conventional cutting methods.

On the other hand, AWJ becomes deflected and rebounded when striking a target material, because of its liquid form. This makes it difficult to control the AWJ for a desired geometry of cut. Striation marks and taper of cuts are major features found in the kerfs when using AWJ for slit cutting [7]. The problem becomes more pronounced when using AWJ for other forms of machining operations, such as milling. Unlike the use of the solid milling tool whose engagement with the workpiece can be made with a desired and constant depth of cut during the process, an AWJ when performing a non-through cut is engaged gradually with the workpiece to form a depth of cut. As the jet penetrates deeper into the material for material removal, it releases the kinetic energy and becomes weaken at its downstream. While the wall of the milled feature is formed by the portion of the jet that contains higher than the destructive energy, the surface profile at the bottom of the cut is affected by a draining flow sweeping on the surface [8]. In addition, the width of the milled feature needs to be properly controlled. To produce a wide channel or pocket in AWJ milling, the jet needs to travel in multiple directions in a multiple pass mode, driven by means of a robot system [9]. This process involves an acceleration and deceleration process to achieve the desired motion of the nozzle. As a result of the momentum conservation, the change in the jet moving direction at the turning points induces an external force acting on the jet [10]. This force intensifies the system vibration and results in an unstable cut, particularly at the edges close to the milled feature walls. Depending on the type of the workpiece material, the erosion can be in the chip formation mode [11] or the crack growth mode [6] or a combination of both. Such a complex variation of the flow affects the milled feature geometry as well as its surface finish. The control of the AWJ-milled feature nowadays still relies mainly on the technique proposed by Hashish [12], where a masking plate made from a hard material is used and material under un-masked areas is eroded to form features. In addition to the cost on making the masks which are not reusable, this method is applicable mainly on the machining of simple features.

In a recent study [13], an AWJ milling technique has been developed. By controlling the jet motion in a stitching trajectory and by tilting the nozzle axis with respect to the machining surface, this technique allows an open channel to be milled at a controlled depth without the need of using a masking plate. An examination of the milled surface morphology has revealed a complex variation of the jet flow resulted from this milling setup, namely, a secondary viscous flow generated when the jet impacts the material surface, a turbulent flow developed during the penetration of the jet into material, a transition or laminar flow at the downstream of the jet and a vortex and damping flow caused by the accumulation of the low-energy solid particles at the bottom of the channel. Because of the complex relation of the multi-variables involved, mathematical formulae conducted by simply correlating the experimental data are unrealistic and cannot reflect the physics embedded. It is thus necessary to develop a quantitative prediction based on the understanding of the mechanisms involved with a sufficient accuracy, to enable this milling

technique to be readily applicable in practice with a controlled depth.

This paper presents an analysis of the AWJ-milled feature formation process through an experimental study. A dimensional analysis is then carried out to relate the material removal rate (MRR) and the geometry of the milled channel to the processing parameters and work material properties, based on the understanding of the effect of jet flow characteristics, the dynamics of nozzle motion and the associated erosion mechanisms. The model is then verified by comparing the model predictions with the corresponding experimental data.

2 Experiment

Figure 1 shows the milling experiment setup. The experiment was conducted on a waterjet cutting system equipped with a Flow Model 5X intensifier pump and an ABB IRB2400 6-axis robot positioning system. The nozzle axis was tilted by an angle (α) from the x-axis in the X–Z plane. The work material was brittle soda–lime glass with a low ductility index (h) of 0.25, compared with δ=0 for diamond and 1 for lead [14]. Its mechanical properties are given in Table 1. The specimen dimension was 50×50×19 mm. Channels were milled on the surface of 50×19 mm with the programmed dimension of 10 mm width (w) and 40 mm length (l).

In this study, five major and easy-to-control process parameters were considered, as shown in Table 2, each of which was set at multiple levels relevant to those commonly used in practice and within the machine specification [13]. Other parameters, i.e. orifice diameter (d_r=0.254 mm), nozzle diameter (d_n=0.76 mm), nozzle length (l_n=76.2 mm), garnet abrasive particles (80 mesh with the average diameter of 0.18 mm) and particle mass flow rate ($_p$=3 g/s) were kept constant. The cross feeds of 0.57, 0.665 and 0.76 mm in fact correspond,

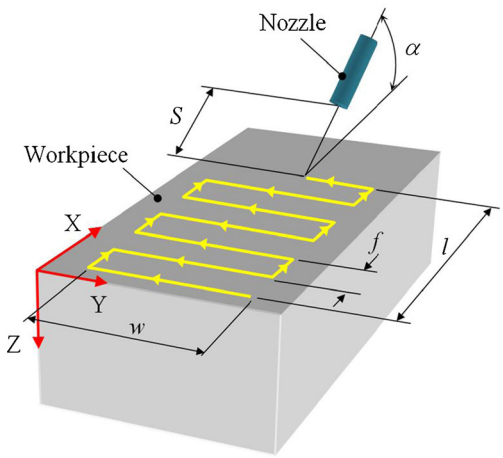

Fig. 1 Setup of the milling experiment

Table 1 Properties of the specimen material (soda–lime glass)

Modulus of elasticity (E (GPa))	73
Tensile strength (σ (MPa))	9.3
Compressive strength (σ' (MPa))	248
Poisson's ratio (ν)	0.22
Vicker hardness (H (GPa))	5.75
Fracture toughness (K (MPa mm$^{1/2}$))	0.75
Thermal conductivity (κ (W/mK))	1.05
Density at 21 °C (ρ (kg/m^3)	2500

respectively, to 0.75, 0.875 and 1.0 times the nozzle diameter. Three sets of tests were conducted, each considering some or all the selected parameters given in Table 2. The first set was for studying the effect of individual operating parameters on the channel geometry, in which the five operating parameters in Table 2 were tested when one other parameter was changed in three levels, forming 15 test runs (detailed combinations will be shown later in Fig. 4). The second set included an orthogonal array for the three levels of nozzle traverse speed, standoff distance, cross feed and nozzle tilt angle, which were then tested with the three water pressures, resulting in 27 test runs. All the 42 test runs were considered in the modelling analysis. The third set of tests was for model verification and will be presented later in the paper.

The channel geometric quantities, i.e. the depth of cut, top channel width and channel wall inclination angle were obtained with the assistance of Nikon C6 Shadowgraph with a ×10 magnification lens and a large display screen. Each quantity on each sample was measured three times, and the average was taken as the final reading.

3 Characteristics of milled channels

Figure 2 shows the typical profile of a milled channel from this study. The channel viewed from the Y–Z plane (see Fig. 1 for the coordinates) can be approximated as in a symmetric trapezoid shape. The top width of the channels (W) is in fact greater than the programmed width (w) by approximately a jet diameter, i.e. $W \approx w + d_j$ (which can be compensated in process planning) and the channel width reduces from the top to the

Table 2 Experimental parameters

Nozzle traverse speed (u ((mm/s))	8, 29 and 50
Water pressure (P (MPa))	100, 125 and 150
Nozzle tilt angle (α (deg))	30°, 40° and 50°
Standoff distance (S (mm))	20, 25 and 30 mm
Cross feed (f (mm))	0.57, 0.665 and 0.76 mm

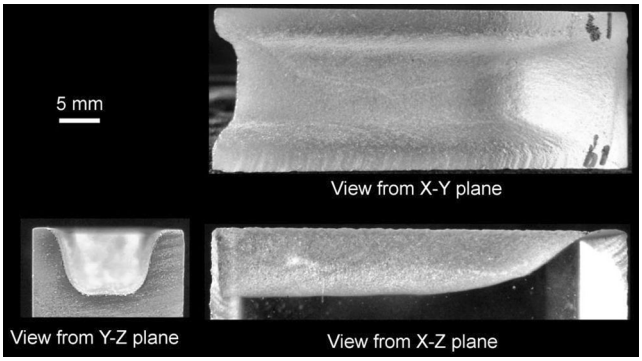

Fig. 2 Typical profile of a milled channel (pressure P=100 MPa; nozzle tilt angle α=50 °; traverse speed u=8 mm/s; standoff distance S=30 mm; and cross feed f=0.665 mm)

bottom along the channel depth so that a wall inclination angle (ϕ) is formed. Round corners (shown as R_1 and R_2 in Fig. 3) are found at the top and bottom of the channel walls, respectively. When viewed from the X–Z plane, the depth of the channel produced by this nozzle tilting milling method reaches to its constant value of depth D after a certain feeding motion in the X direction (i.e. $D\cot\alpha$ approximately). The calculation of MRR is considered in the steady-state range of ($L \geq x \geq L - D\cot\alpha$), i.e.

$$\mathrm{MRR} = \frac{A}{t_o} \tag{1}$$

where A is the cross-sectional area in the Y–Z plane of the channel and t_o is the time required for milling a unit distance in the X direction. The cross-sectional area, A, is determined by

$$A = A_0 + A_1 - A_2 \tag{2}$$

where A_0, A_1 and A_2 are the areas of the portions shown in Fig. 3, in which A_0 is the area of the trapezoid. Equation (2) can thus be re-written as,

$$A = D(W - D\tan\phi) + 2\left(R_1^2 - R_2^2\right)\left[\tan\left(\frac{\pi}{4} - \frac{\phi}{2}\right) - \left(\frac{\pi}{4} - \frac{\phi}{2}\right)\right] \tag{3}$$

As shown in Fig. 3, since R_1 and R_2 are small as compared with D, and $R_1 \approx R_2$, Eq. (3) becomes

$$A \approx A_0 = D(W - D\tan\phi) \tag{4}$$

The time, t_o, is determined as

$$t_o = \frac{W + f}{fu} \tag{5}$$

where the symbols are as defined in the Nomenclature. Combining Eqs. (1), (4) and (5) yields

$$\mathrm{MRR} = \frac{D(W - D\tan\phi)fu}{W + f} \tag{6}$$

The effect of the process parameters on the channel geometry is shown in Fig. 4. To obtain a channel with a desired geometry, it requires a simultaneous selection of the various operating parameters. For instance, a low water pressure may be used to generate a shallow channel. However, this results in a larger channel wall inclination angle (Fig. 4a). It is encouraging that an

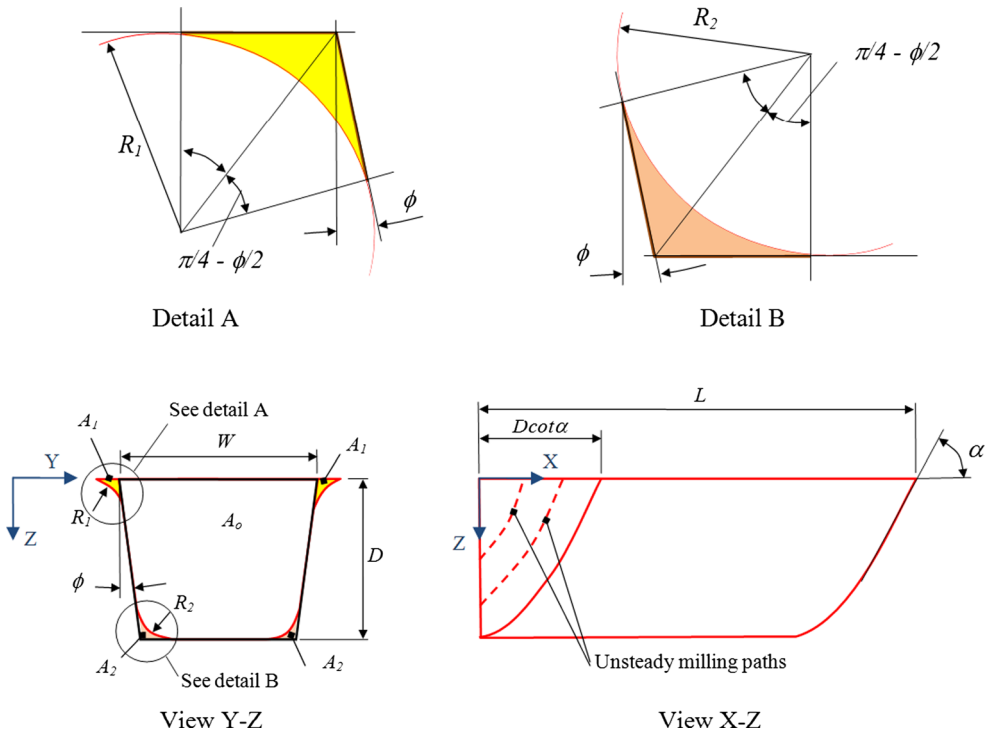

Fig. 3 Schematic of channel geometry used in the analysis

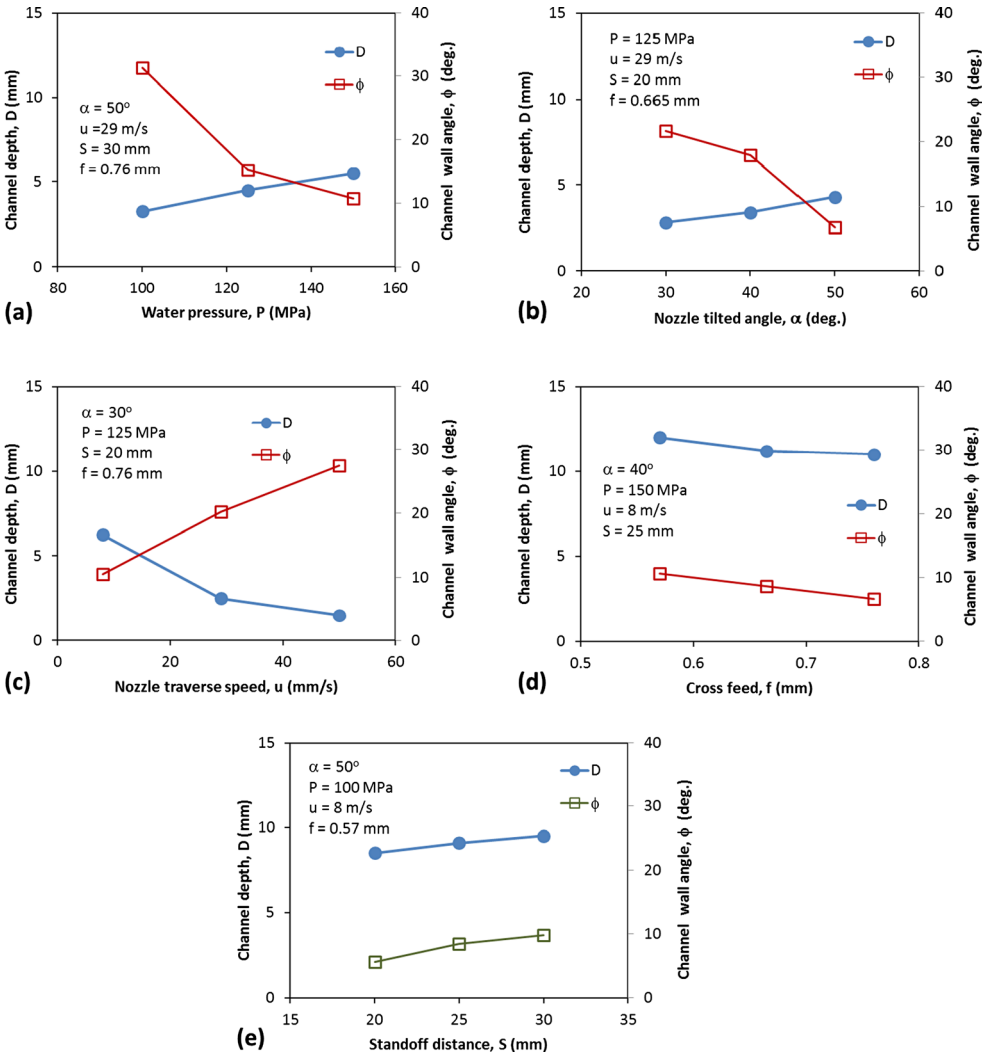

Fig. 4 Effect of process parameters on the channel geometry

increase in the nozzle tilt angle results in an increase in the channel depth and a decrease in the channel wall angle (Fig. 4b); however, it makes the control of the depth more difficult. By contrast, a reverse trend is applied as the traverse speed is increased, as shown in Fig. 4c. The relations between the channel geometry and the other operating parameters such as the cross feed (Fig. 4d) and standoff distance (Fig. 4e) follow different trends with different gradients. The effect of the operating parameters on the channel formation is in fact a result of the material response to the erosion process, predominantly the jet flow (or impacting particle) characteristics and the dynamics of nozzle motion. These are discussed below.

4 Analysis of milled channel formation

4.1 Impact erosion

The impact erosion mainly takes place by the interaction between the energy-carrying particles and the target material in AWJ machining. Since the abrasive particles are much harder than the target material (i.e. hardness of the garnet particle is 20.6 GPa, compared with 5.75 GPa of the target glass), it is not unreasonable to assume that there is no deformation in the abrasive particles when impacting the target material [15]. The impact of a particle results in two force components, i.e. an indenting force normal to the work surface and a force tangential to the surface. The indenting force pushes the particle to impinge the workpiece, and at the same time, the tangential force may create micro-chips during the motion of the particle or cause material damage by tension-related failure. Depending on the threshold value of the material to initiate a crack and the attribution of the two force components in action, material removal mechanisms may be classified into ductile deformation or brittle fracture [16]. When a particle impacts a given target material with a low kinetic energy or at a shallow angle, the impact is unable to initiate cracks in the target material and ductile mode erosion may take place [17]. Under the ductile erosion mode, material experiences some or a combination of the rubbing, ploughing

and cutting actions to form a displaced volume, as shown in Fig. 5. It is postulated that the displaced volume (V_i) is propositional to the kinetic energy carried by a particle that has a mass (m_p) and initial impact velocity (v_p), i.e.

$$\frac{1}{2}m_p v_p^2 \propto C_e \int_0^h \int_0^b A_{yz}(x)A_{xy}(z)\mathrm{d}x\mathrm{d}z = C_d V_i \tag{7}$$

where h is the total penetration depth, b is the total sliding distance, $A_{yz}(x)$ and $A_{xy}(z)$ are respectively the projected areas of particle on the Y–Z and Z–Y planes at the position of x and z, and C_e is the coefficient considering the response of material to the impact of particle under elastic–plastic deformation [16] and is given by

$$C_e = C_e(H, E) \tag{8}$$

in which H and E are the hardness and Young's modulus of the target material, respectively

During the penetration, the motion of a particle is distorted by an angle φ_p. It is obvious that the trajectory of the particle in the x and z domain is greatly influenced by the particle attack angle (α_p) in the relation of

$$z = z(x, H, \alpha_p) \tag{9}$$

Under the brittle erosion mode shown in Fig. 6, upon the particle impact, a fragmentation or damaged zone that consists of a complex network of cracks with random sizes and locations is generated [18]. The cracks are propagated by the sliding motion of particle that also scoops the fragments away from the zone. Therefore, the normal component of the kinetic

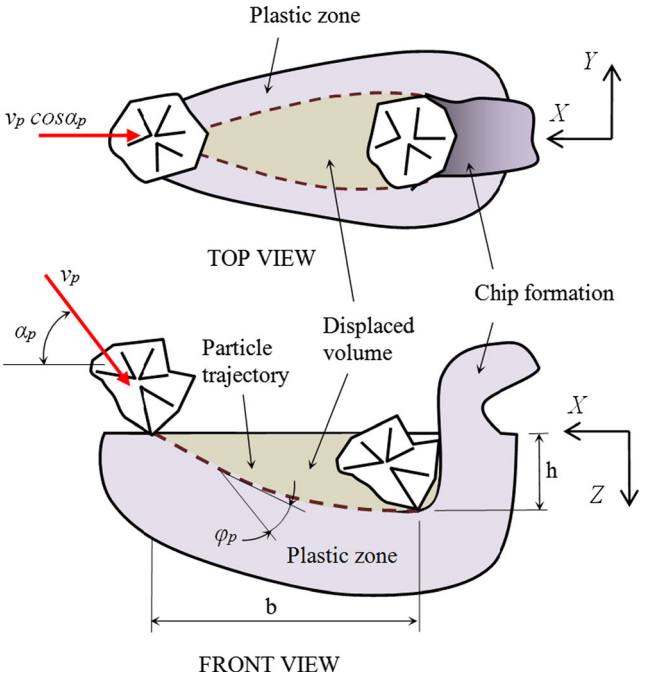

Fig. 5 Material removal by oblique impact of a particle in ductile mode

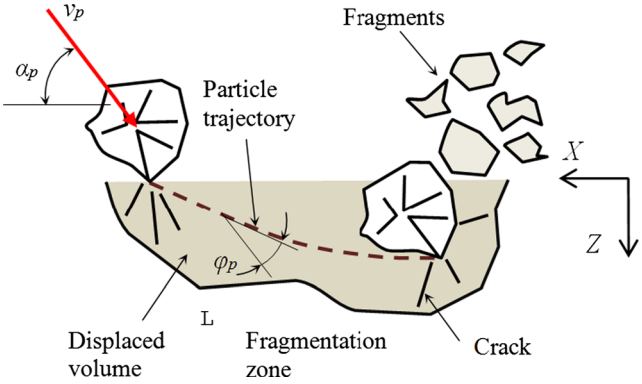

Fig. 6 Material removal by oblique impact of a particle in brittle mode

energy that initially applies on the target material under this erosion mode becomes a major cause for the erosion. It is postulated that the total volume of all fragments removed under this erosion mode (V_i) is propositional to the kinetic energy of the impacting particle [19], i.e.

$$\frac{1}{2}m_p\left(v_p \sin\alpha_p\right)^2 \propto \frac{K^2}{E}V_i^{2/3} \tag{10}$$

where K is the fracture toughness of the target material.

In AWJ machining, particle fragmentation exists; however, for micro-sized solid garnet particles, the overall change to the particle size is small [20]. To simplify the analysis, particle fragmentation is not considered in this study. By taking the nominal particle size for the particles used, the number of particles ejecting from the nozzle can be given by

$$\dot{n} = \frac{\dot{m}_p}{m_p}, \tag{11}$$

where $\dot{m}_p$ is the mass flow rate of particles flowing through the nozzle exit and m_p is the average particle mass.

The MRR can be approximated as

$$\mathrm{MRR} = \psi_c \psi_v \psi_u \sum_{i=1}^{\dot{n}} V_i \tag{12}$$

It is noted that there are three major factors that should be considered in the evaluation of the MRR. Firstly, due to the fact that the liquid carrying the particles is splashed upon the impact [21] and the particles in the jet-target material interface may collide with each other, not all the particles ejecting from the nozzle exit will play, or have enough energy to play, a role in the erosion. Secondary, the velocity of particles varies across the jet cross section and along the jet downstream during the development of flow (as will be discussed in Sect. 4.2), which according to Eqs. (7) and (10) will alter the effect or contribution of particles to the erosion process. Finally, since the jet velocity decreases at its downstream, the jet at a certain downstream distance becomes unstable and eventually is unable to penetrate into the bulk material.

In fact, the nozzle traverse speed determines the jet exposed time, which together with the jet characteristics relating to the jet trajectory determine the material erosion (as will be discussed in Sect. 4.3) and the variation of MRR for a given target material. The coefficients of ψ_c, ψ_v and ψ_u in Eq. (12) account for the above three effects.

The MRR may be considered to be associated with the rate of kinetic energy of an AWJ, which is given as

$$\frac{\mathrm{d}KE}{\mathrm{d}t} = C_s \frac{1}{2} \dot{m}_s \bar{v}_j^2 \tag{13}$$

where $\bar{v}_j$ is the average velocity of the AWJ at the particle-target material interface, which for k number of particles in the cross section of the jet can be given by:

$$\bar{v}_j = \frac{1}{k} \sum_{i=1}^{k} v_i \tag{14}$$

and C_s is the factor accounting for the reduction of the jet velocity in a distance from the nozzle exit to the impact site, which may be expressed as

$$C_s = C_s(S, \xi, \alpha, \varphi) \tag{15}$$

where S is the standoff distance, ξ is the distance from the workpiece surface to where the particles undertake the erosion, α is the nozzle tilted angle (or jet impact angle) and φ is the angle of jet deflection when penetrating into the material and can be expressed as

$$\begin{cases} \varphi(\mathbf{z})|_{\mathbf{z}=\mathbf{0}} = \mathbf{0} \\ \lim\limits_{\mathbf{z}\to\mathbf{D}} \varphi(\mathbf{z}) = \boldsymbol{\alpha} \end{cases} \tag{16}$$

For the AWJ injection system used in this study (as shown in Fig. 7), after mixing with particles, $\bar{v}_j$ can then be found by using the momentum transfer equation

$$\bar{v}_j = C_m \left(\frac{\dot{m}_w}{\dot{m}_s} \right) \bar{v}_w \tag{17}$$

where C_m is the momentum transfer efficiency, $\dot{m}_s$ and $\dot{m}_w$ are the mass flow rates of mixture slurry through the focussing tube and the water through the orifice, respectively, which from the law of mass conservation, are in the relation of

$$\dot{m}_s = \dot{m}_w + \dot{m}_p \tag{18}$$

The average velocity of waterjet flowing through the orifice ($\bar{v}_w$) can be determined by applying the Bernoulli's equation, i.e.

$$\bar{v}_w = C_d \left(\frac{2P}{\rho_w} \right)^{1/2}, \tag{19}$$

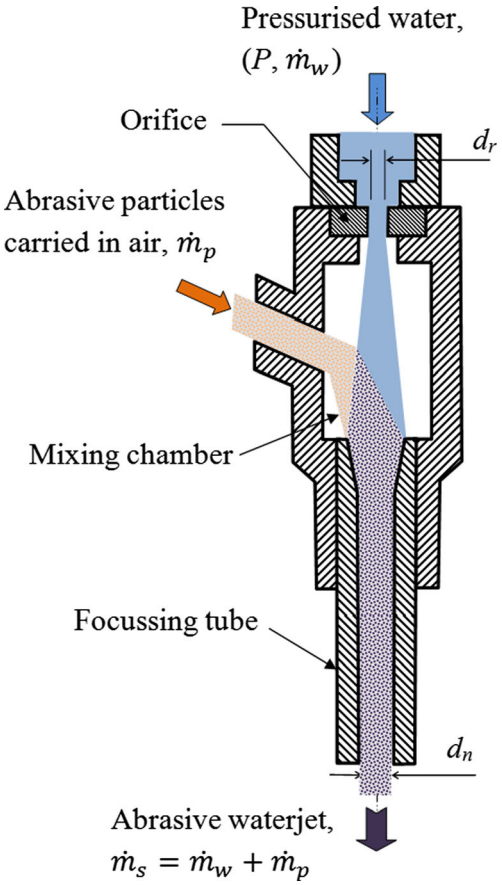

Fig. 7 The formation of an abrasive waterjet [34]

where P is the water pressure, ρ_w is the water density and C_d is the discharge coefficient that accounts the momentum losses due to nozzle wall friction and fluid-flow disturbances, which according to Chen and Geskin [22] can be taken approximately at 0.87 for the water pressure of 100–250 MPa considered in this study.

By simultaneously solving Eqs. (13), (17), (18) and (19), the equation for the rate of kinetic energy of an AWJ becomes

$$\frac{\mathrm{d}KE}{\mathrm{d}t} = C_s C_m^2 C_d^2 \left(\frac{\dot{m}_w^2}{\dot{m}_w + \dot{m}_p} \right) \left(\frac{P}{\rho_w} \right) \tag{20}$$

From the continuity condition for a steady incompressible flow, the flow rate $\dot{m}_w$ is determined by

$$\dot{m}_w = \pi \frac{d_r^2}{4} \rho_w \bar{v}_w \tag{21}$$

where d_r is the diameter of the orifice. Substituting Eq. (19) into Eq. (20) gives

$$\dot{m}_w = C_d \frac{\pi}{2\sqrt{2}} d_r^2 (P \rho_w)^{1/2} \tag{22}$$

From the above analysis, the MRR can be expressed as

$$\mathrm{MRR} = \mathrm{MRR}\left(\psi_c, \psi_v, \psi_u, C_s, C_m, C_d, S, \zeta, H, K, E, \alpha, P, d_r, \dot{m}_p, \rho_w\right) \tag{23}$$

Since the channel characteristics are implicitly resulted from the MRR, the channel depth (D) and the wall inclination angle (ϕ) can also be expressed as functions of the independent variables in Eq. (23).

4.2 Jet flow characteristics

In AWJ machining, water is used to accelerate and carry solid particles to erode the material. The formation of channel features depends strongly on the development of jet flow, as found in a previous work [13], progresses through different stages.

Upon an impact, not all the jet volume can perform the cutting action, and a portion of it is rebounded. Apart from the splashes or mists formed [21], the remaining acts as a viscous flow sliding on the workpiece surface and away from the site of impact [23]. The particles enclosed become dynamically unstable, and rotates with high angular velocity [24]. The shear induced by the viscous flow and the rotating particles acts to open a cut by rounding off the channel edges.

The major portion of jet that penetrates into the material at an initial stage is of high velocity. Its flow is formed as a turbulent stream that involves with a development of a boundary layer, growing when the fluid flows over the wall surface, as shown in Fig. 8. There is a momentum exchange of the viscous fluids that flow between the region near the jet axis and that close to the channel wall when progressing to the stage of fully developed turbulent velocity profile [25]. This results in an increase in the material erosion at the jet axis region, while that at the channel wall decreases, thus forming an inclination of the channel wall. The erosion takes place mainly via the cutting wear mode by particles of high velocity [26, 27].

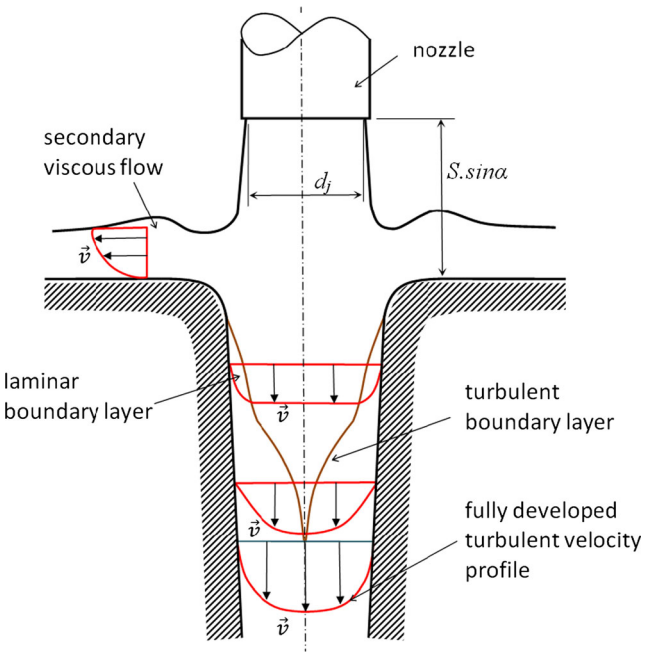

Fig. 8 Flow developed during a jet impact, viewed from YZ plane in Fig. 1

As the jet penetrates deeper into the material, it releases the kinetic energy and becomes weaken. At a certain penetrating depth, the turbulent flow no longer exists and is replaced by a transition or laminar flow [13]. Since AWJ milling is a non-through cutting process, the erosion in the bottom of the channel may be changed to the deformation wear mode [12], in which the accumulation of solid particles at the bottom of the channel that follow a vortex and damping flow may become a dominant material removal mechanism [28]. In this zone, the jet is more vulnerable to external influences such as mechanical vibrations caused by the acceleration/deceleration of the moving nozzle, which will be discussed in the next section.

The above analysis indicates the importance of the viscous behaviour of an AWJ on the erosion process when subjected to the change of inertia force caused by the variation of velocity developed through the jet body. Such behaviours of the viscous flow can be generally represented by the Reynolds number, i.e.

$$Re = \frac{\rho_s \overline{v}_j d_j}{\mu_s} \tag{24}$$

where $\overline{v}_j$, as defined above, is the average jet velocity at the jet-target material interface, ρ_s is the density of mixture of water and particles, d_j is the diameter of the jet which at a small distance of $S\sin\alpha+\xi$ can be approximated as the nozzle diameter and μ_s is the fluid viscosity.

It is noted that the abrasive-water slurry is a non-Newtonian fluid and its dynamic fluid viscosity can be presented by the following equation [29]:

$$\mu_s = K_\mu \dot{\gamma}^{n-1} \tag{25}$$

where $\dot{\gamma}$ is the shear rate; and the constitutive properties of the fluid, K_μ and n, are defined as the indexes of consistency and flow behaviour, respectively, and can be expressed as [29], i.e.

$$K_\mu = K_\mu\left(C_p, d_p, \mu_w\right) \tag{26}$$

$$n = n\left(C_p, d_p\right) \tag{27}$$

where d_p is the nominal particle diameter, μ_w is the viscosity of water and $C_p = \dot{m}_p/\dot{m}_s$ is the particle concentration in the slurry, in which $\dot{m}_s$ can be determined using Eqs. (18) and (22).

According to Valko and Economides [30], for a given controlled volume, the shear rate ($\dot{\gamma}$) is a function of the jet velocity at the impact zone, i.e.

$$\dot{\gamma} = \dot{\gamma}\left(\bar{v}_j\right) \tag{28}$$

Therefore, from Eqs. (26), (27) and (28), the dynamic viscosity of the slurry can be given by

$$\mu_s = \mu_s\left(\mu_w, C_p, d_p, \bar{v}_j\right) \tag{29}$$

For the AWJ nozzle system used in this study, from Eqs. (17), (18) and (22), and according to the analysis in Sect. 4.1, the coefficient ψ_v can be expressed as:

$$\begin{aligned}\psi_v &= \psi_v(\mu_s)\\ &= \psi_v\left(\psi_s, \psi_d, \psi_m, C_s, C_m, C_d, \rho_w, \mu_w, \dot{m}_p, d_p, P, d_r\right)\end{aligned} \tag{30}$$

4.3 Dynamics of nozzle motion

Unlike in the AWJ cutting of slits where the cutting wall is formed continuously by the movement of the jet, the milled channel, often wider than the jet diameter, is formed by superimposition of a number of discrete milling passes. In this milling technique, the channel is achieved by controlling the motion of nozzle in a stitching trajectory (Fig. 1). At the turning points of the motion track where the direction of motion is changed sharply about 90°, the nozzle needs to decelerate to zero before the directional change and then accelerates from zero velocity to reach the desired traverse speed (u). Figure 9 shows a sketch of the movement of a jet to perform the milling. The jet is enclosed by a control volume (V_{cv}) that moves with an acceleration of $d^2\vec{R}/\mathrm{d}t^2$ related to a reference frame XYZ fixed to the workpiece. As a result of the momentum conservation, to resist such dynamic changes of the control volume, an additional force ($\vec{F}$) will be induced in the direction opposite to the acceleration, as presented by the equation below [10].

$$\vec{F} - \int_{V_{cv}} \rho_s \left(\frac{d^2\vec{R}}{\mathrm{d}t^2}\right)\mathrm{d}V = \frac{\partial}{\partial t}\int_{V_{cv}} \rho_s \vec{v}_j \mathrm{d}V + \oint_{A_{cv}} \rho_s \vec{v}_j \left(\vec{v}_r . \vec{n}\right)\mathrm{d}A, \tag{31}$$

where $\vec{R}$ is the position vector of the moving control volume (xyz), and A_{cv} is the control surface area, i.e. cross section of the jet.

The force $\vec{F}$ created causes a deflection of the moving jet. Since the sidewall of the channel is formed by superimposing the jet action at the beginning and the end of each traverse motion or pass, the jet deflection directly results in the wall inclination. This action also plays a role in the formation of the channel depth. The nozzle speed affects the time that the jet exposes to the material when moving in the X direction, and consequently affects the number of abrasive particles that impinge a given area of the cutting front.

From this analysis, the coefficient ψ_u introduced in Eq. (23) to account for the effect of nozzle motion can therefore be expressed as

$$\psi_u = \psi_u\left(\rho_s, v_j, d_j, a, f, u\right) \tag{32}$$

which according to Eqs. (17), (18) and (22) can be re-written as

$$\psi_u = \psi_u\left(C_m, C_d, d_r, P, \rho_w, \dot{m}_p, d_j, a, f, u\right) \tag{33}$$

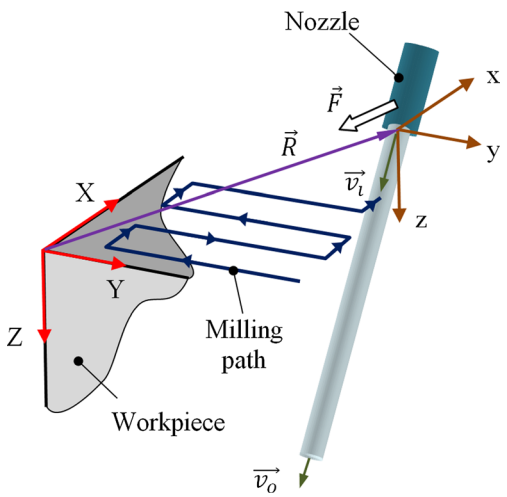

Fig. 9 An analytical control volume of an AWJ during feed motion

5 Predictive models

The coefficient ψ_c introduced in the foregoing analysis is to consider the particle–particle interaction in the fluid stream, the random nature of particles impacting on the target and the splashing of liquid upon the impact of jet on a solid target. However, there is little understanding of these phenomena. Similarly, the ψ_v and ψ_u have been introduced to account for the variation of velocity within the flow stream and the non-Newtonian viscosity that are very complex to be determined numerically. It is thus difficult to develop a purely mathematical model to characterise the AWJ milling process that is practically applicable. It is noticed that the dimensional analysis can often give very satisfactory formulae for the quantitative prediction of a wide range of machining processes, in particular where the causes for machining mechanisms are well understood, e.g. [31, 32]. The aforementioned analysis as expressed by Eqs. (13), (30) and (31) indicates that the geometry of the channel is a result of the operating parameters that

influence the jet kinetic energy (S,P,α, $_p,\rho_s$), the dynamics of the moving nozzle (a, u, f), the target material properties to resist the erosion (H,K,E), and the dynamic viscous property of slurry (μ_s) that causes a variation of the jet flow behaviour across the jet and along the jet flow direction. For a given AWJ system, the nozzle configuration (C_s, C_m, C_d and d_r) can be approximated as constant and water is commonly used as a liquid media in which ρ_w and μ_w are unchanged. The depth of channel (D) therefore can be expressed in a general form as

$$D = D\left(S, P, \alpha, a, u, f, d_n, \dot{m}_p, d_p, H, K, E\right) \tag{34}$$

Following the Buckingham theorem, the relationship in Eq. (34) can be presented in a dimensionless form as

$$f(\Pi_1, \Pi_2, \ldots, \Pi_{10}) = 0 \tag{35}$$

By selecting d_n, u and P as the repeating parameters, the corresponding dimensionless parameters in Eq. (35) can be given as

$$f\left(\frac{D}{d_n}, \frac{S}{d_n}, \sin\alpha, \frac{ad_n}{u^2}, \frac{f}{d_n}, \frac{\dot{m}_p u}{{d_n}^2 P}, \frac{d_p}{d_n}, \frac{H}{P}, \frac{K}{P{d_j}^{1/2}}, \frac{E}{P}\right) = 0. \tag{36}$$

The physical meanings of the dimensionless groups in Eq. (36) may be summarised as:

- $\Pi_1 = D/d_n$ is the dependent parameter, representing the relative channel depth over the nozzle diameter,
- $\Pi_2 = S/d_n$ represents the effect of the standoff distance in relative to the nozzle diameter,
- $\Pi_3 = \sin\alpha$ indicates the effect of the nozzle tilt angle,
- $\Pi'_4 = \Pi_4\Pi_5 = af/u^2$ represents the effect of dynamic stability of nozzle motion,
- $\Pi'_5 = 1/\Pi_5 = d_n/f$ represents the effect of the nozzle diameter in performing a small feed,
- $\Pi'_6 = \Pi_6/\Pi_5^2 = \dot{m}_p u/f^2 P$ indicates the effect of machining parameters in the nozzle motion trajectory,
- $\Pi_7 = d_p/d_n$ represents the size effect of particles within the cross section of a jet,
- $\Pi_8 = H/P$ reflects the effect of material hardness to resist the erosion in the ductile mode,
- $\Pi_9 = E/P$ reflects the effect of material's Young modulus to resist the erosion in both the ductile and brittle modes, and
- $\Pi'_{10} = \Pi_{10}^2/\Pi_9^2 = E^2 d_n/K^2$ reflects the effect of material properties to resist the brittle fracture upon the impact of a jet from a nozzle of diameter d_n.

Equation (36) can be re-written as

$$\frac{D}{d_n} = f_D\left(\frac{S}{d_n}, \sin\alpha, \frac{af}{u^2}, \frac{d_n}{f}, \frac{\dot{m}_p u}{f^2 P}, \frac{d_p}{d_n}, \frac{H}{P}, \frac{E}{P}, \frac{E^2 d_n}{K^2}\right). \tag{37}$$

Similarly, the dependent parameters for channel wall angle can be expressed in the dimensionless form as:

$$\cos\phi = f_\phi\left(\frac{S}{d_n}, \sin\alpha, \frac{af}{u^2}, \frac{d_n}{f}, \frac{\dot{m}_p u}{f^2 P}, \frac{d_p}{d_n}, \frac{H}{P}, \frac{E}{P}, \frac{E^2 d_n}{K^2}\right) \tag{38}$$

Finally, the MRR can be computed using Eq. (6) where the parameters D and ϕ are obtained from Eqs. (37) and (38), respectively.

6 Model verification

6.1 Assessment of model predictability

Equations (37) and (38) can be developed into applicable equations by using the power-law formulation where variables that are constant in a particular application can be implicitly accounted for as a coefficient. Thus, for the glass (whose properties are given in Table 1) used in this study Eqs. (37) and (38) can be respectively expressed as

$$D = C_D\, S^{\zeta_1}(\sin\alpha)^{\zeta_2}\left(\frac{f}{u^2}\right)^{\zeta_3}\left(\frac{1}{f}\right)^{\zeta_4}\left(\frac{u}{f^2 P}\right)^{\zeta_5}\left(\frac{1}{P^2}\right)^{\zeta_6} \tag{39}$$

$$\cos\phi = C_\phi S^{\chi_1}(\sin\alpha)^{\chi_2}\left(\frac{f}{u^2}\right)^{\chi_3}\left(\frac{1}{f}\right)^{\chi_4}\left(\frac{u}{f^2 P}\right)^{\chi_5}\left(\frac{1}{P^2}\right)^{\chi_6} \tag{40}$$

The 42 sets of experimental data as described in Sect. 2 have been used to evaluate the constants (coefficients and exponents) in Eqs. (39) and (40). The ranges of the variables covered in the models are (the units of the parameters are given in the Nomenclature):

$$10 \le S\sin\alpha \le 30, \text{ where} \tag{41}$$

$$60^\circ \ge \alpha \ge 30^\circ; \text{ and} \tag{42}$$

$$u \le 50, \tag{43}$$

$$f \le 0.76. \tag{44}$$

The lower limit in Eq. (41) was to avoid a vigorous splashing that may interfere with the layer of the secondary viscous flow and results in large round-off edges of the channel as discussed earlier. Because of the diversion of a jet when ejecting through the nozzle, the upper limit in Eq. (41)

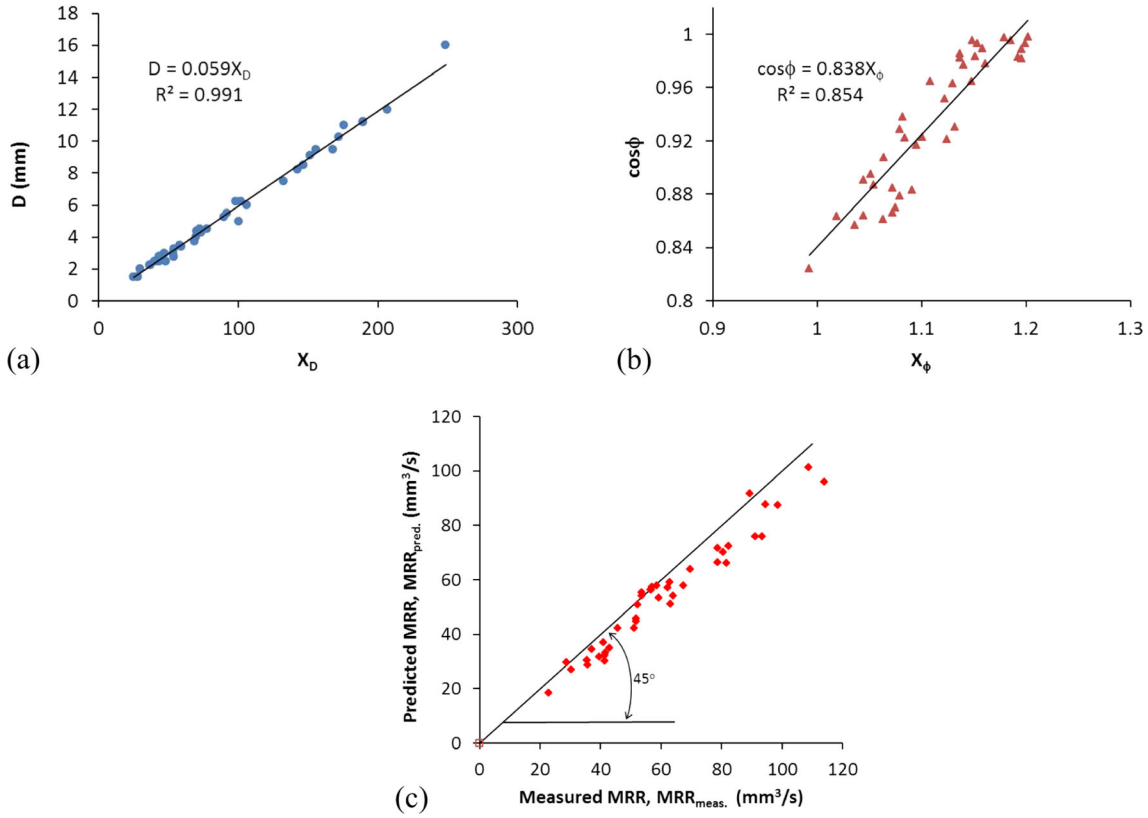

Fig. 10 Regression analysis: **a** channel depth, **b** channel wall inclination angle and **c** material removal rate

considered the largest distance at which the nozzle diameter can be taken approximately as the jet diameter at the target surface. The conditions in Eqs. (43) and (44) were to avoid the bulge pockets that occur at the bottom corners of the milled channel [13] due to the unstable motion of the nozzle.

Using the multi-variable regression at a 95 % confidence level, the power-law relations are obtained as follows.

$$D = 0.059S^{0.148}(\sin\alpha)^{1.232}\left(\frac{f}{u^2}\right)^{3.241}\left(\frac{1}{f}\right)^{-7.768}\left(\frac{u}{f^2P}\right)^{5.791}\left(\frac{1}{P^2}\right)^{-3.546} \quad (45)$$

or

$$D = 0.059\,S^{0.148}(\sin\alpha)^{1.232}f^{-0.573}u^{-0.692}P^{1.301} = 0.059X_D \quad (46)$$

and

$$\cos\phi = 0.838S^{-0.105}(\sin\alpha)^{0.156}\left(\frac{f}{u^2}\right)^{-0.506}\left(\frac{1}{f}\right)^{-1.442}\left(\frac{u}{f^2P}\right)^{0.963}\left(\frac{1}{P^2}\right)^{-0.551} \quad (47)$$

or

$$\cos\phi = 0.838S^{-0.105}(\sin\alpha)^{0.156}f^{0.022}u^{-0.049}P^{0.139} == 0.502X_\phi \quad (48)$$

where the units of the parameters are given in the Nomenclature. The MRR can be predicted using Eq. (6) in which D and ϕ are obtained from Eqs. (46) and (48), respectively.

Figure 10a and b show that the measured values of D and ϕ correlated well with the models in Eqs. (46) and (48), respectively. A good agreement was found with the R-squared values of 0.991 and 0.854 for D and ϕ, respectively. A comparison

Table 3 Experimental channel geometry and MRR using the operating parameters determined from the Microsoft Excel Solver with the developed models to mill a channel on a glass (target channel depth D=8 mm and wall angle $\phi \leq 5$ °)

Operating parameters (a, P, u, S, f)[a]	Channel depth (mm)	Channel wall inclination angle (deg)		Experimental MRR (mm³/s)
	Experiment	Experiment	Converged solution	
(60, 100, 10.7, 25.7, 0.64)	7.7	2.7	4.1	93.6
(60, 125, 18.5, 26.4, 0.56)	8.2	3.5	5.0	91.0
(55, 150, 25.1, 29.2, 0.56)	7.9	4.5	5.0	87.1
(60, 150, 27.1, 25.2, 0.56)	8.1	5.3	5.0	87.3

[a] Units are given in the Nomenclature

between the measured and predicted values of MRR is given in Fig. 10c which again shows small discrepancies. The model will be further assessed below when used for selecting the process parameters.

6.2 Parameter selection consideration

The foregoing analyses and models in Eqs. (46) and (48) can be used for selecting the operating parameters (α, P, u, S, f) to obtain a desired channel geometry, within the ranges of the parameters specified in Eqs. (41)–(44). This is illustrated by an example below.

Example To determine the operating parameters for milling on the given glass to obtain a channel with the width and depth of 12×8 mm and the wall angle less than 5 °.

It is noted that since five variables (α, P, u, S, f) are to be determined with only two independent equations (Eqs. (46 and 48), there is not a unique solution for this problem. The solutions may be obtained using the Generalised Reduced Gradient (GRG2) Algorithm [33] available in the Microsoft Excel *Solver*. The examination of the partial gradients ($\partial D/\partial x$ and $\partial\varphi/\partial x$, where x is the operating parameter) in Eqs. (46) and (48) shows that the most influential parameters for the channel geometrical parameters, D and ϕ, are P and α. However, to cater for practical convenience in adjusting these two parameters, the input of P and α into the programme was made at the increment of 5 MPa and 1°, respectively. With the targeted depth of cut D=8 mm and by applying the constraint of $\cos\phi \geq \cos(5\ °)$ together with the constraints in Eqs. (41)–(44), the converged solutions and the corresponding experimental MRRs have been found and are given in Table 3. The discrepancies between the results obtained by the model and from experiment are small with less than 3.8 % for the channel depth and ±1.5° for the wall inclination angle. It is interesting to notice from Table 3 that when the water pressure is at 100 MPa (the lowest), the MRR is the largest. This indicates that in this controlled-depth milling, merely increasing the water pressure may not always be able to increase the MRR.

7 Conclusions

An analysis of the channel formation mechanisms in the controlled-depth AWJ milling of a brittle glass has been presented. The study has revealed that the channel formation in the AWJ milling technique is predominately affected by the impact of the erosion process, the jet flow characteristics and the dynamics of nozzle motion. The erosion takes place by the interactions between solid particles and the target material and can occur in both the ductile and brittle mode, depending on the particle attack angle and velocity and the material properties. On the other hand, the motion of particles is driven by the flow of jet in which the velocity profile varies across the jet diameter and along the jet downstream. The dynamic stability of the nozzle motion in the stitching trajectory plays an important role in the formation of the channel wall. Relevant equations were developed to represent the effects of the process parameters on the key factors that govern the channel formation, including the jet kinetic energy, the dynamics motion of the nozzle, the target material properties to resist the erosion and the dynamic viscous property of slurry that affects the jet flow behaviour. Based on the analysis and using a dimensional analysis approach, predictive models have then been developed for the major machining performance measures, including MRR, channel depth and channel wall inclination angle. The experimental verification has shown that the model predictions are in good agreement with the corresponding experimental data.

Acknowledgement This project was supported by the Australian Research Council under the Linkage-Projects scheme.

References

1. Nguyen T, Zhang LC (2005) The coolant penetration in grinding with segmented wheels—part 1: mechanism and comparison with conventional wheels. Int J Mach Tools Manuf 45(12–13):1412–1420. doi:10.1016/j.ijmachtools.2005.01.035
2. Axinte DA, Karpuschewski B, Kong MC, Beaucamp AT, Anwar S, Miller D, Petzel M (2014) High energy fluid jet machining (HEFJetmach): from scientific and technological advances to niche industrial applications. CIRP Ann Manuf Technol 63(2):751–771. doi:10.1016/j.cirp.2014.05.001
3. Momber AW, Kovacevi R (1998) Principles of abrasive water jet machining. Springer, London
4. Arola D, McCain ML, Kunaporn S, Ramulu M (2001) Waterjet and abrasive waterjet surface treatment of titanium: a comparison of surface texture and residual stress. Wear 249(10–11):943–950. doi:10.1016/S0043-1648(01)00826-2
5. Wang J (1999) Abrasive waterjet machining of polymer matrix composites—cutting performance erosive process and predictive models. Int J Adv Manuf Technol 15(10):757–768. doi:10.1007/s001700050129
6. Momber AW, Eusch I, Kovacevic R (1996) Machining refractory ceramics with abrasive waterjet. J Mater Sci 31:6485–6493. doi:10.1007/BF00356252
7. Hashish M (1991) Characteristics of surfaces machined with abrasive-waterjet. Eng Mater Tech 113:354–362. doi:10.1115/1.2903418
8. Kong MC, Anwar S, Billingham J, Axinte DA (2012) Mathematical modelling of abrasive waterjet footprints for arbitrarily moving jets: part I—single straight paths. Int J Mach Tools Manuf 53:58–68
9. Anwar S, Axinte DA, Becker AA (2013) Finite element modelling of overlapping abrasive waterjet milled footprints. Wear 303(1–2):426–436. doi:10.1016/j.wear.2013.03.018
10. Gerhart P, Gross R, Hochstein J (1992) Fundamentals of fluid mechanics, 2nd edn. Addison-Wesley Publishing Company, Boston

11. Wang J (2003) Abrasive waterjet machining of engineering materials. Trans Tech Publications, Uetikon-Zuerich, Switzerland
12. Hashish M (1998) Controlled depth of milling of isogrid structures with AWJs Transaction of ASME. J Manuf Sci Eng 120:21–27. doi:10.1115/1.2830106
13. Dadkhahipour K, Nguyen T, Wang J (2012) Mechanisms of channel formation on glasses by abrasive waterjet milling. Wear 292–293:1–10. doi:10.1016/j.wear.2012.06.008
14. Rabinowicz E (1995) Friction and wear of materials, 2nd edn. Wiley, New York
15. Fowler G, Pashby IR, Shipway PH (2009) The effect of particle hardness and shape when abrasive water jet milling titanium alloy Ti6Al4V. Wear 266(7–8):613–620. doi:10.1016/j.wear.2008.06.013
16. Hutchings IM (1992) Tribology friction and wear of engineering materials. Edward Arnold, London, UK
17. Wensink H, Elwenspoek MC (2002) A closer look at the ductile-brittle transition in solid particle erosion. Wear 253(9–10):1035–1043. doi:10.1016/S0043-1648(02)00223-5
18. Bowden F, Field J (1964) The brittle fracture of solids by liquid impact, by solid impact, and by shock. Proc R Soc Lond Ser A Math Phys Eng Sci 282:331–352
19. Yasser MA, Wang J (2011) Impact abrasive machining. In: Jackson MJ, Davim JP (eds) Machining with abrasives. Springer, New York, USA
20. Li WY, Wang J, Zhu HT, Li HZ, Huang CZ (2013) On ultrahigh velocity micro-particle impact on steels—a single impact study. Wear 305:216–227. doi:10.1016/j.wear.2013.06.011
21. Allen RF (1988) The mechanics of splashing. J Colloid Interface Sci 124(1):309–316. doi:10.1016/0021-9797(88)90352-9
22. Chen WL, Geskin ES (1990) Measurement of the velocity of abrasive waterjet by the use of laser transit anemometer. In: 10th International Symposium on Jet cutting technology, Amsterdam, Netherlands. Elsevier Applied Science, pp 23–36
23. Rochester MC, Brunton JH (1972) High speed impact of liquid jets on solid. Paper presented at the First International Symposium on Jet Cutting Technology,
24. Humphrey JAC (1990) Fundamentals of fluid motion in erosion by solid particle impact. Int J Heat Fluid Flow 11(3):170–195. doi:10.1016/0142-727X(90)90036-B
25. Cengel YA, Cimbala JM (2009) Fluid mechanics: fundamentals and applications. 2nd edn. McGraw-Hill,
26. Bitter JGA (1963) A study of erosion phenomena, part 1. Wear 6(1):5–21. doi:10.1016/0043-1648(63)90003-6
27. Bitter JGA (1963) A study of erosion phenomena, part 2. Wear 6(3):169–190. doi:10.1016/0043-1648(63)90073-5
28. Pang KL, Nguyen T, Fan J, Wang J (2012) A study of micro-channeling on glasses using an abrasive slurry jet. Mach Sci Technol 16(4):547–563. doi:10.1080/10910344.2012.731947
29. Tanner R (2000) Engineering rheology, 2nd edn. Oxford University Press, New York
30. Valko P, Economides M (1995) Hydraulic fracture mechanics. John Wiley & Sons, Chichester, England
31. Nguyen T, Shanmugam DK, Wang J (2008) Effect of liquid properties on the stability of an abrasive waterjet. Int J Mach Tools Manuf 48(10):1138–1147. doi:10.1016/j.ijmachtools.2008.01.009
32. Nguyen T, Zhang LC (2005) Modelling of the mist formation in a segmented grinding wheel system. Int J Mach Tools Manuf 45(1):21–28. doi:10.1016/j.ijmachtools.2004.06.019
33. Lasdon LS (1985) Nonlinear programming algorithms-applications, software, and comparisons. In: Boggs PT, Byrd RH, Schnabel RB (eds) Numerical optimization 1984. In: Proceedings of the SIAM Conference on Numerical Optimization, 1984. Philadelphia: SIAM, pp 41–70
34. Shanmugam DK, Nguyen T, Wang J (2008) A study of delamination on graphite/epoxy composites in abrasive waterjet machining. Compos A: Appl Sci Manuf 39(6):923–929. doi:10.1016/j.compositesa.2008.04.001